

# Self-noise Effects on Aerodynamics of Cambered Airfoils at Low Reynolds Number

Tomoaki Ikeda\*, Takashi Atobe†

*Japan Aerospace Exploration Agency (JAXA), Tokyo, 182-8522, Japan*

and

Daisuke Fujimoto‡, Ayumu Inasawa§ and Masahito Asai¶

*Department of Aerospace Engineering, Tokyo Metropolitan University, Tokyo 191-0065, Japan*

Aerodynamics of cambered airfoils are investigated numerically, using NACA four-digit series of 6% thickness at low Reynolds number  $Re = 10,000$ , and moderate Mach number  $M = 0.2$ , by focusing on the relation of aeroacoustic effects and hydrodynamic flow unsteadiness. Two-dimensional numerical simulations show that the onset of an acoustic feedback loop (AFL) leads to an abrupt increase in lift force. Associated with the feedback process, the evolution of two-dimensional vortices in the suction-side boundary layer shifts a separation bubble toward the leading edge, which causes a relatively steep pressure recovery near the trailing edge. Through a parametric study on airfoil shape, the aerodynamically favorable feature of aft camber is further enhanced with the presence of an AFL. In addition, the aft camber airfoil successfully forms a laminar separation bubble in three-dimensional calculations at the present Reynolds number, developing transitional behavior on the suction side, supposedly prompted by the airfoil tones. Although the boundary layer shows three-dimensional complexity, still the formation of an AFL is strongly suggested, via the comparison of spanwise correlations.

## I. Introduction

For low-speed, small unmanned aerial vehicles, suited for hobby use or surveillance activity, the Reynolds number  $Re$  based on flight velocity and airfoil chord length reduces down to the order of  $10^5$  or less. Due to the laminarization of the flow near airfoil surface, the boundary layer would easily separate at small angle of attack, with only a moderate adverse pressure gradient. The aerodynamic performance of an airfoil is lowered significantly, and also depends greatly on Reynolds number. These low-Reynolds-number characteristics modify an airfoil design process which has been established on the assumption of a mostly attached, turbulent boundary layer at sufficiently high Reynolds number. The flight in low atmospheric density, such as ultra high-altitude cruise at 20–30 km from sea level, also attracts the concern of aerodynamics at low Reynolds number [1, 2, 3]. Since dynamic pressure reduces due to low atmospheric density, airfoil design needs additional care to attain required operational lift at a target range of Reynolds number, at relatively

---

\*Research Associate, Aerodynamics Research Group.

†Associate Senior Researcher, Aerodynamics Research Group.

‡Graduate Student.

§Associate Professor.

¶Professor.

high flight velocity, where compressible effects should be considered as well. For instance, since the atmospheric density at 30 km high reduces down to 1/100 of that at the surface level, the chord-length Reynolds number of a small aircraft could be the order of  $10^4$ , or possibly even lower, at the altitude in subsonic flight. More recently, Mars atmospheric flight has been of engineering interest for scientific research as similar low-Reynolds-number environments [e.g., 4, 5].

It is often distinctively discussed that a laminar separation bubble formed on the suction side has a great effect on aerodynamic performance at low Reynolds number [e.g., 6, 3, 7]. Once a laminar boundary layer separates behind the leading edge, the separated shear layer is highly receptive, and may cause laminar-turbulent transition, depending on various conditions, such as Reynolds number, instability of the shear layer, receptivity and magnitude of external disturbances, and so on. Then, the resultant turbulent shear layer induces reattachment somewhere on the chord. As a crude estimation, the lower bound of Reynolds number is proposed as about  $5 \times 10^4$  to form a laminar separation bubble [1, 8]. At this Reynolds number, the numerical work by [9] closely investigated the receptivity of acoustic disturbances on a laminar separation bubble formed on the suction side of an NACA0012 airfoil, concluding that the aerodynamic noise reproduced in their direct simulation was a sufficient stimulus for transition.

At even lower Reynolds number, still acoustic effects can be non-negligible on aerodynamic characteristics at moderate Mach numbers. In a numerical study of present authors [10], trailing-edge noise causes acoustic resonance via the instability mechanism of a separated boundary layer, forming an acoustic feedback loop (AFL) at  $Re = 10^4$ . The acoustic pressure is rather amplified through the resonance, acting as unsteady force exerted on the surface. At moderate Reynolds number, the onset conditions of an AFL have been studied both experimentally and numerically [e.g., 11, 12, 13, 14, 15, 16, 17, 18], as a major tonal noise emitted from airfoil flow. In our case at  $Re = 10^4$ , however, the shedding frequency may become as low as the order of one, normalized by chord length and mean velocity. The lower frequency variation has a further impact on the aerodynamic characteristics of airfoil design. Although the presence of airfoil camber reduces the instability of a boundary layer [10], an AFL is still prompted by increasing an angle of attack.

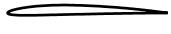
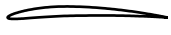
In this paper, we conduct a parametric study of aerodynamic characteristics using cambered four-digit NACA airfoils. We would focus on the camber effect and its relevance with aeroacoustic resonance, by altering maximum camber height and its location, at  $Re = 10,000$ . A higher-order computational code is employed to directly solve compressible Navier-Stokes equations, including aeroacoustic phenomena. Then, acoustic resonance should be reproduced properly. To consider aeroacoustic effects, low, but moderate inflow Mach number,  $M = 0.2$  is employed throughout this paper in numerical simulations.

## II. Numerical Conditions and Approaches

In the present study, NACA four-digit airfoils with 6% thickness are examined. The parameter set of four digits represents maximum camber height, its location, and maximum thickness, for this family of NACA airfoils. At low Reynolds number, it is well known that a thinner airfoil should exhibit a better aerodynamic performance [19, 20]. However, from a practical point of view, a certain level of thickness must be ensured to attain minimal structural strength. Here, 6% of chord length is provided as the airfoil maximum thickness. In two-dimensional numerical simulations, four maximum camber heights and locations are parametrically studied, respectively: as maximum camber height, 2%, 4%, 6%, and 8% of chord length; as the location of maximum camber height, 20%, 40%, 60%, and 80% chord. Therefore, the present parametric study covers a

16-point matrix of NACA 4-digit series, also for a range of angles of attack:  $\alpha = 0^\circ\text{--}10^\circ$ . Airfoil configurations are summarized in Table 1. In addition, an uncambered NACA0006 airfoil is used as a reference [10].

**Table 1. NACA four-digit cambered airfoils examined in the present study.**

	x206	x406	x606	x806
2x06				
4x06				
6x06				
8x06				

By using a computational code, compressible Navier-Stokes equations are solved. Fluid property is assumed to be of air; its specific-heat ratio is treated to be constant, 1.4. The chord length  $L$  is used as the characteristic length scale. The trailing edge of each airfoil is placed at the origin in the two-dimensional,  $x$ - $y$  coordinates. The airfoil is tilted by the angle of attack,  $\alpha$  to the streamwise,  $x$  direction. The uniform flow  $U_\infty$  is enforced in the  $x$  direction at the outer boundaries. The Reynolds number based on  $L$  and  $U_\infty$  is chosen to be 10,000. In the normalization of numerical quantities,  $L$  and  $U_\infty$  are employed, unless otherwise noted. The mean-flow Mach number of the present simulations is fixed at  $M = 0.2$ , as mentioned in the introduction. In addition to the global  $x$ - $y$  coordinates, we introduce the local  $X$ - $Y$  coordinates, whose origin comes to the leading edge, and  $X$  axis is aligned to the chord direction. They will be used when the distribution near the airfoil is of interest, regardless of angle of attack. The schematic of geometrical configurations is shown in Fig. 1.

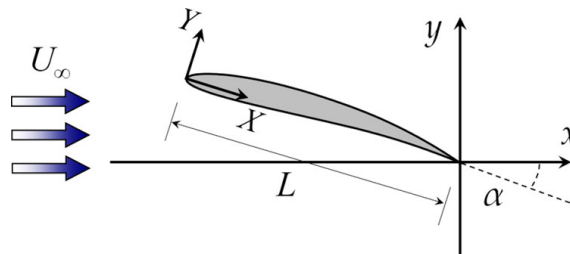


**Figure 1. Schematic of numerical configurations.**

For spatial discretization, a C-grid topology is employed by applying a tri-diagonal sixth-order compact scheme to both convection and viscous terms. A standard fourth-order Runge-Kutta scheme is implemented for time advancement. The numerical domain is extended to  $20L$  in both the radial and downstream directions with a non-reflecting boundary condition applied to all outer boundaries. Also to minimize unfavorable acoustic reflection, a sponge layer [21] is introduced for about  $3L$  from the boundaries. The details of the implementation of numerical schemes and the verification studies of the present computational code are summarized in [22]. In a two-dimensional parametric study, the number of grid cells is 800 in the circumferential direction (400 around the airfoil surface; 400 in the wake region) and 200 in the wall normal direction, which leads to  $1.6 \times 10^5$  cells for two-dimensional grid. Grid convergence was confirmed

by monitoring the resultant unsteady aerodynamic forces and the variance of velocity field on various grid sizes on two-dimensional cases.

In only limited cases, we also conducted three-dimensional calculations. The cases are selected by inspecting the two-dimensional results of the 16-point matrix at relatively high angles of attack,  $\alpha \geq 7^\circ$ . At a lower angle of attack, flow is expected to be practically two-dimensional. In the spanwise direction, a periodic boundary condition is imposed with the length  $1L$ , discretized by 128 cells. The number of cells around the airfoil surface is increased to 600, and numerical cells are closely clustered on the upper surface to resolve three-dimensional eddies if any arise; approximately  $2/3$  of the cells are gathered on the upper side of the airfoil. In total,  $2.6 \times 10^7$  numerical cells are employed in the three-dimensional cases. The minimum cell height is  $1 \times 10^{-3}L$  adjacent to the wall. In wall units, the normalized height is less than 1 on the suction side of the airfoil, whereas the normalized cell widths in the chord and spanwise directions are less than 5 and 8, respectively. As will be shown later, resolved eddies can be seen in the region within about  $0.3L$  in the wall-normal direction, from the suction-side surface. The maximum wall-normal cell height in the region is about  $0.01L$ , which corresponds approximately to 10 in wall units.

### III. Summary of the Results

We conducted two-dimensional compressible flow simulations for 16 cambered airfoils, varying angle of attack  $\alpha$  from  $0^\circ$  to  $10^\circ$  with one degree increments; 176 cases were run in total. Most cases show unsteadiness with vortex shedding except for a few with the smallest camber height of 2% chord length, at low angles of attack. To reach a sufficiently developed unsteady state, usually 20–30 non-dimensional time was necessary. However, when an AFL formed very slowly, some cases required more than 100 non-dimensional time to achieve a final state.

As three-dimensional simulations, we only ran the following 8 cases: NACA4606 and 6806 at  $\alpha = 7^\circ$ ; NACA4202, 4406, and 4806 at  $\alpha = 8^\circ$ ; NACA4406, 4806 and 8606 at  $\alpha = 10^\circ$ . As for initial states, instantaneous flow fields of corresponding two-dimensional results were employed. To initiate three-dimensional flow motions, sufficiently small amplitude of volumetric forcing, composed of several temporal and spanwise Fourier modes, was applied near the leading edge, for about first 2 non-dimensional time. Owing to the instability in the suction-side boundary layer and the wake, the synthetic disturbance grows spatially. Then, after the forcing is turned off, self-sustaining three-dimensional flow may develop if the boundary layer bears adequate instability for given spanwise fluctuations. If sufficiently random three-dimensional motions develop, it can be considered as a statistically independent state which should not depend on initially added forcing modes. In the present case, 20–30 non-dimensional time was run before statistical samples were taken in the three-dimensional simulations. However, in the cases of NACA4606 and 6806 at  $\alpha = 7^\circ$ , as three-dimensional disturbances gradually decayed, two-dimensional states were retrieved eventually. Since inadequate spanwise length of computational domain often damps three-dimensional motions, it was extended up to  $4L$  in the two cases, to confirm that only two-dimensional motions were maintained in the present numerical conditions.

### IV. Unsteadiness of Two-dimensional Flow

In our previous numerical study [10], airfoil tones were examined for NACA0012, 0006 and 4406 airfoils, by changing angles of attack. Here, primary vortex shedding frequencies are summarized for the present airfoils, sampled at  $0.1L$  above the trailing edge, as well as NACA0006 in Fig. 2. In the figure, only non-zero,

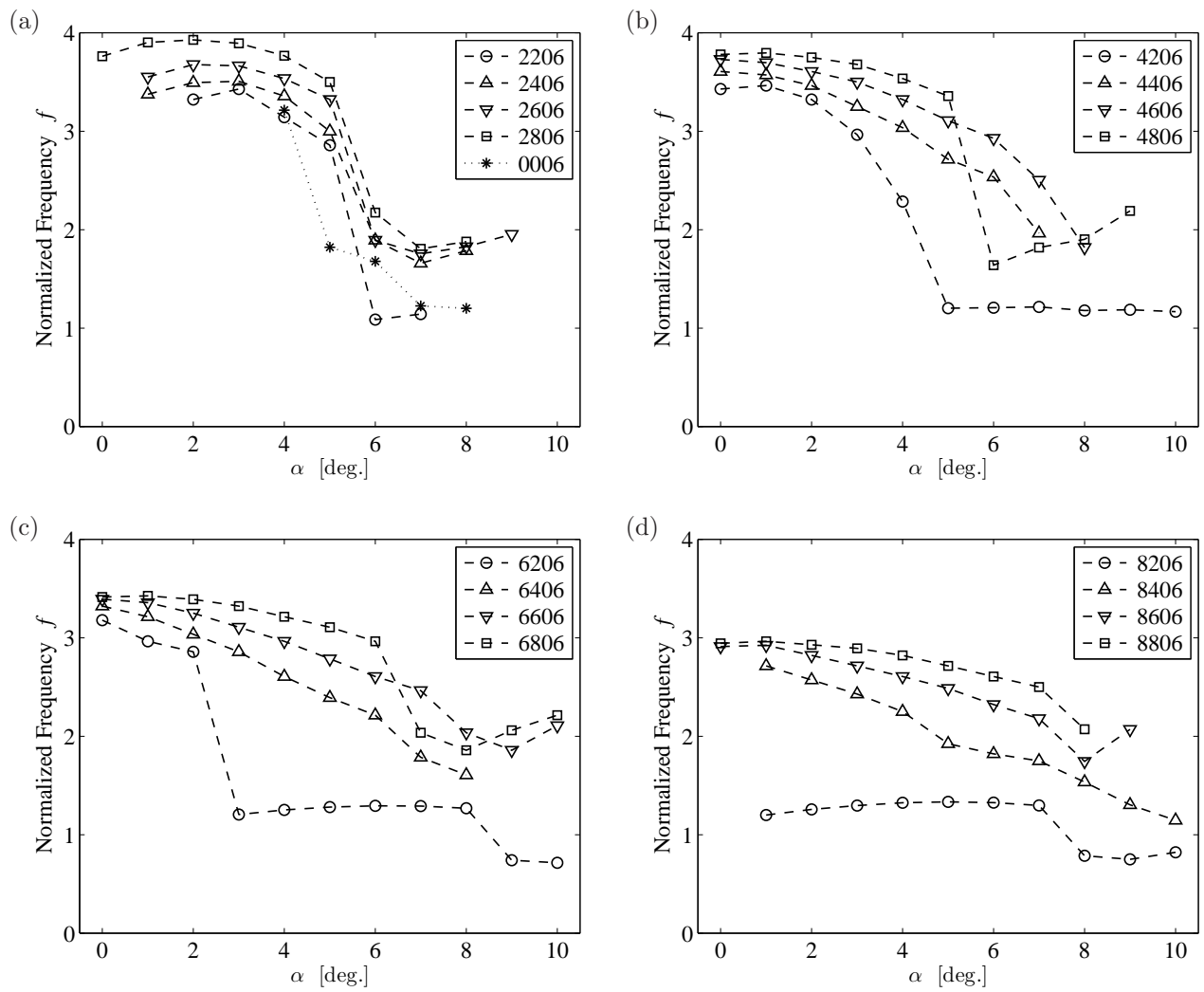
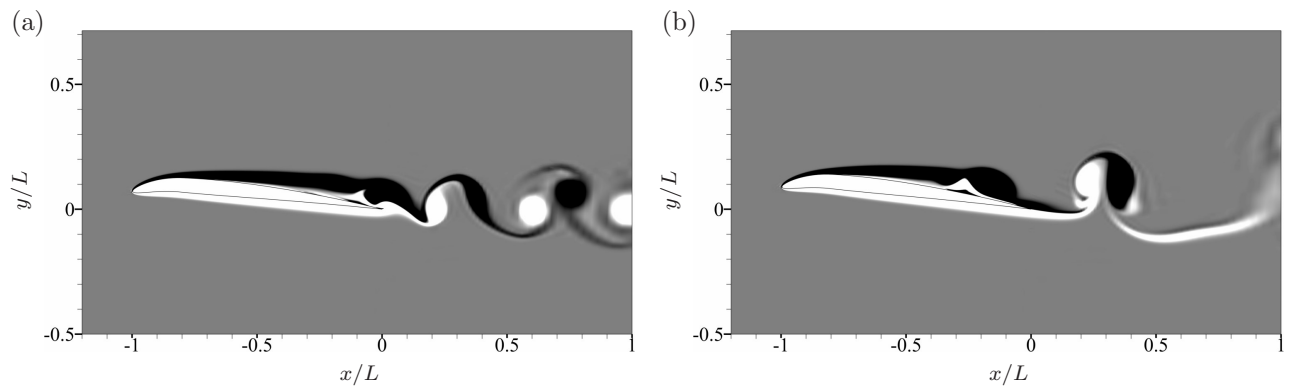
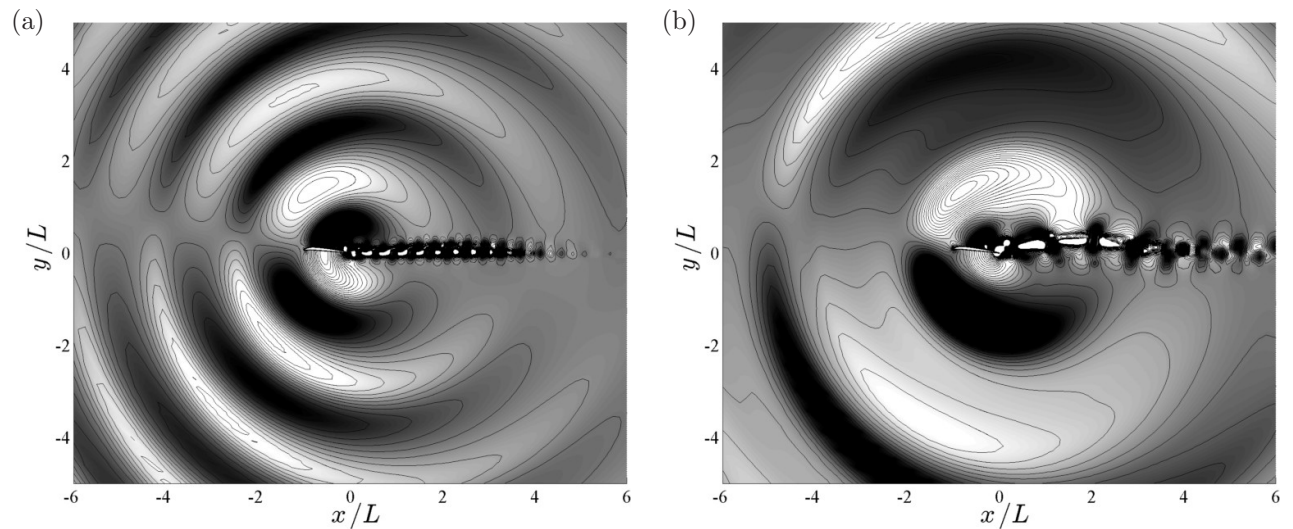


Figure 2. Primary vortex shedding frequencies sampled at  $0.1L$  above the trailing edge of: (a) NACA2x06 and 0006; (b) 4x06; (c) 6x06; (d) 8x06 airfoils.



**Figure 3.** Instantaneous  $\omega_z$  vorticity distributions of NACA4206 airfoil at: (a)  $\alpha = 4^\circ$ ; (b)  $\alpha = 5^\circ$ . Gray scale ranges between  $-5 \leq \omega_z L/U_\infty \leq +5$  from black to white.



**Figure 4.** Instantaneous pressure fluctuations of NACA4206 airfoil at: (a)  $\alpha = 4^\circ$ ; (b)  $\alpha = 5^\circ$ . Gray scale ranges between  $-1 \times 10^{-2} \leq p'/\rho_\infty U_\infty^2 \leq +1 \times 10^{-2}$  from black to white. Superposed contour lines denote the pressure difference  $\Delta p' = 2 \times 10^{-3} \rho_\infty U_\infty^2$ .

primary peak frequencies are shown. In several cases, typically at a higher angle of attack, clear peaks cannot be found in power spectra with irregular vortex shedding. They are excluded from the present figure.

For the symmetric NACA0006 airfoil, vortex shedding patterns drastically change from  $\alpha = 4^\circ$  to  $5^\circ$  at  $M = 0.2$ , along with the formation of an AFL [10]. With the presence of airfoil camber, similar transition still occurs. An example is shown in Fig. 3 for NACA4206 airfoil. At a lower angle of attack  $\alpha = 4^\circ$ , alternating vortex shedding is observed, induced primarily by wake instability with a separation bubble near the trailing edge. By increasing  $\alpha$  to  $5^\circ$ , vortex formation occurs rather upstream as shown in Fig. 3-(b). A pair of closely coupled vortices is formed as shed into the wake, enhancing transverse velocity fluctuations near the trailing edge. This also amplifies the intensity of scattered aerodynamic sound, which is eventually fed back upstream as a hydrodynamic disturbance that develops into an appreciable vortical motion in the boundary layer. This is a typical form of an AFL, reproduced in two-dimensional numerical simulations at the present Reynolds number, 10,000. Associated acoustic scattering, or instantaneous pressure fluctuation  $p'$  is presented in Fig. 4. The onset of an AFL also lowers the shedding frequency due to the difference of instability mechanisms between the wake and the upper-side boundary layer [17]. In Fig. 2-(a), a similar

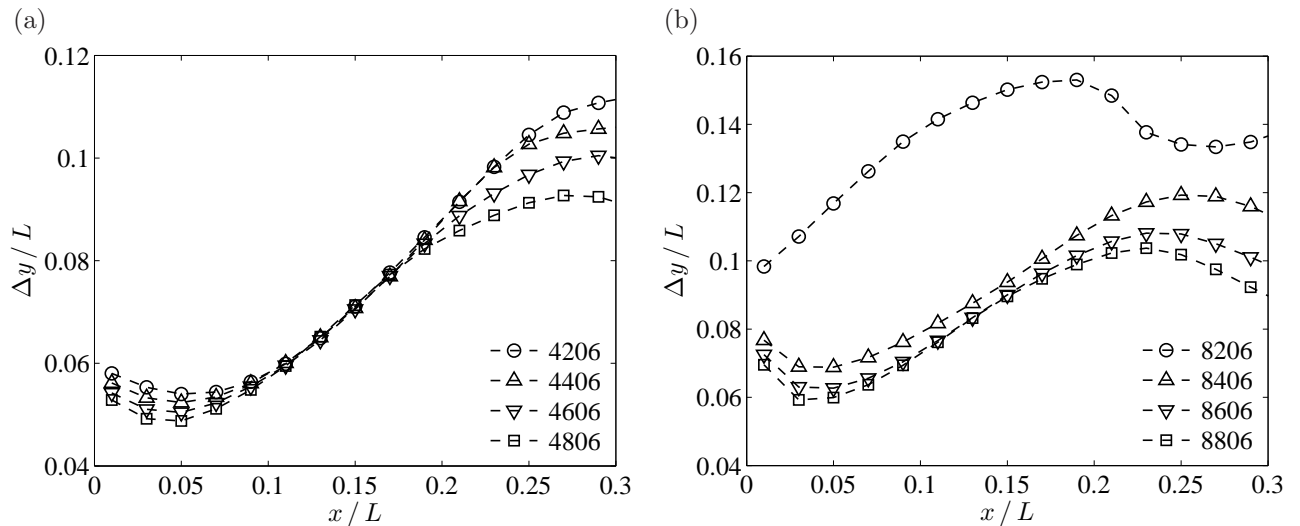


Figure 5. Half width of velocity deficit,  $\Delta y$  measured in the time-averaged wake at  $\alpha = 2^\circ$  for: (a) NACA4x06; (b) NACA8x06.

frequency fall-off can be seen for all other airfoils at  $\alpha = 6^\circ$ .

In fact, the state shown in Fig. 3-(a) at  $\alpha = 4^\circ$  should be considered to be a weak form of an AFL as well, as vortices start to develop in the suction-side boundary layer, which increases the magnitude of acoustic pressure scattered at the trailing edge. As will be shown in Fig. 6, the lift fluctuation becomes already significant at  $\alpha = 4^\circ$ . However, the vortex-shedding pattern observed in the figure strongly suggests the dominant effect of wake instability. The frequency selection mechanism of this case will be discussed in Section V.

By further increasing camber height, however, frequency variation becomes more dependent upon maximum camber location. For the most forward cambered airfoils, NACAx206, the change in vortex shedding patterns occurs at a lower angle of attack, as increasing camber maximum height, shown in Figs. 2-(a) to (d). Furthermore, once an AFL is formed, the shedding frequency seemingly settles at particular discrete values on  $\alpha$ . The set of the most aft cambered airfoils, NACAx806, also shows a relatively clear fall-off, which corresponds to the onset of an AFL. However, the critical angle for the occurrence of an AFL becomes higher as increasing camber height. In other families of camber location, a discontinuous change of frequencies becomes less obvious as camber height increases. In fact, NACA8406 does not show an apparent pattern change in the present range of angles of attack.

We should also notice that the shedding frequencies of aft cambered airfoils are higher than those of forward cambered ones at low angles of attack, compared at the same camber height. As the unsteadiness is governed by the wake instability for small  $\alpha$ , the frequency can be closely correlated with wake width, if a similarity law holds for wake velocity profiles. The aft camber generally restricts the size of a trailing-edge separation bubble, which limits the width of wake velocity deficit. The same reason applies to the frequency decrement, as increasing camber height without the onset of an AFL. To represent the wake width scale, half width of wake velocity deficit is often adopted, as in [23]. Fig. 5 compares the wake parameter in the streamwise direction, for 4% and 8% maximum camber heights at  $\alpha = 2^\circ$ . For NACA4x06 airfoils at the angle of attack, all the cases show a reverse flow region behind the trailing edge, which prompts vortex shedding via wake instability. The half-width profiles are very similar; their local minima simply decrease as

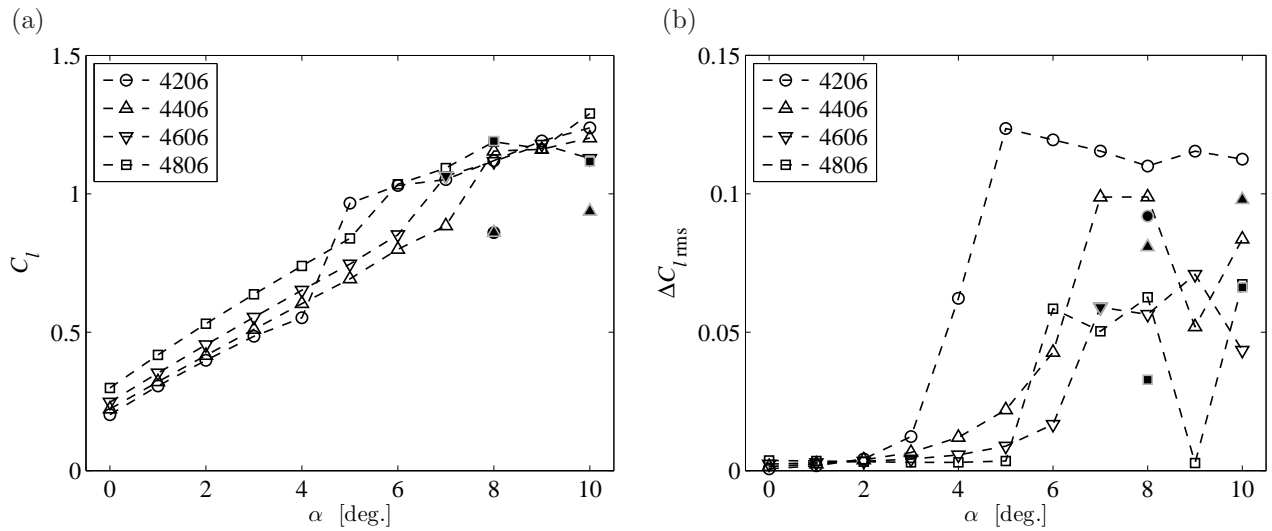


Figure 6. Comparison of lift coefficients between two-dimensional simulation results of NACA4x06 airfoils: (a) time-averaged lift curves; (b) the rms fluctuations. Filled markers denote three-dimensional simulation results.

the maximum camber location moves backward, correspondingly to the increments in the vortex-shedding frequency. For NACA8x06 airfoils, however, only NACA8206 shows a peculiar profile, with no reverse flow in the wake. It is the consequence of direct vortex shedding from the suction-side boundary layer, on the formation of an AFL, as seen in the case of  $\alpha = 5^\circ$  in Fig. 3. The relation between wake velocity profiles and the resultant vortex-shedding frequencies will be examined in more details in Section V.

The onset of an AFL also affects aerodynamic forces acting on airfoil surface. Fig. 6 compares time-averaged lift curves of 4% camber-height airfoils and their rms fluctuations. Lift is approximately linearly proportional to  $\alpha$  at lower angles of attack. However, all four airfoils present discontinuous jumps of lift, between  $\alpha = 5^\circ$  and  $8^\circ$ , which corresponds to the transition of vortex shedding patterns shown in Fig. 3, in the present two-dimensional study. Lift fluctuations are also amplified significantly, simultaneously with, or just before the lift jump. In a low frequency limit, the time derivative of lift is directly associated with far-field sound pressure, perceived as trailing-edge noise. Therefore, the increments in lift fluctuations approximately represent an aerodynamic noise increase. Its quadrupole sound source is primarily the fluctuation of vorticity near the trailing edge, via vortex shedding. Eventually, the rms fluctuation of lift may exceed 10% of lift force itself.

Some of the three-dimensional results are also included in Fig. 6. In the airfoil set of 4% camber height, six cases were run. Among them, NACA4606 at  $\alpha = 7^\circ$ , where the lift jump occurs with the AFL formation, resulted in two-dimensional final state. The other three airfoils were examined at  $\alpha = 8^\circ$ ; two additional runs were performed at  $\alpha = 10^\circ$ . At  $\alpha = 8^\circ$ , similarly to the NACA4606 case at  $\alpha = 7^\circ$ , the aft cambered airfoil NACA4806 successfully reproduces the non-linear lift gain in a three-dimensional simulation, while the lift slightly decreases by further increasing an angle of attack to  $\alpha = 10^\circ$ . On the other hand, the other two forward cambered airfoils significantly decrease the lift, which eventually lowers their aerodynamic performances, compared to the two-dimensional solutions. The AFL, if any exist in these cases, does not help in increasing lift when three-dimensional motions develop. However, the lift fluctuations of the airfoils with forward camber reach nearly 10% of the lift at  $\alpha = 8^\circ$ . Significant aerodynamic sound should be present

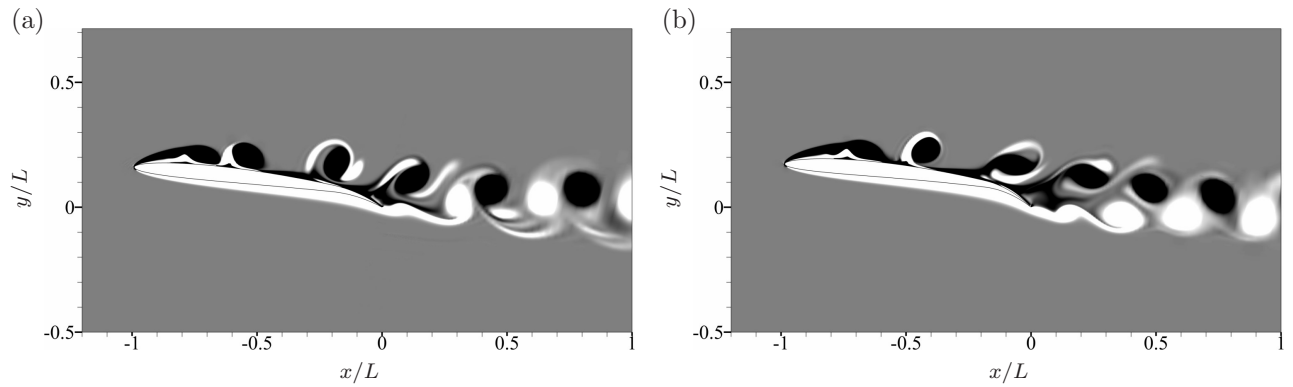


Figure 7. Alternating vortex patterns retrieved at a relatively higher angle of attack: (a) NACA4806 at  $\alpha = 9^\circ$ ; (b) NACA6806 at  $\alpha = 10^\circ$ . Also see the caption of Fig. 3.

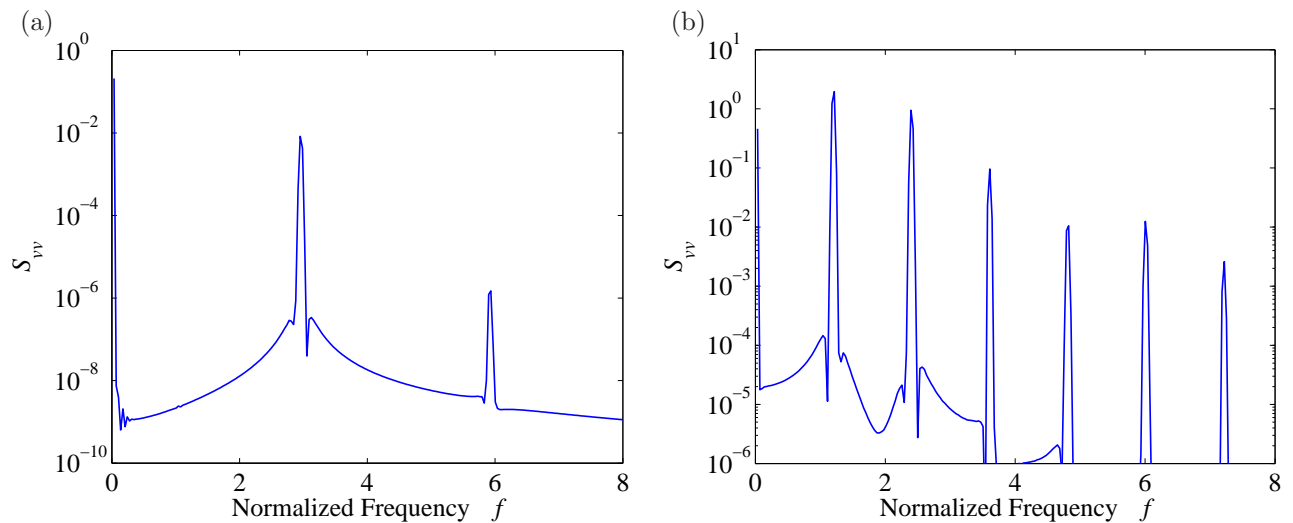


Figure 8. Power spectral density of  $v$ -velocity, sampled at  $0.1L$  above the trailing edge over the non-dimensional time  $30 \leq t \leq 60$ , for NACA4206 at: (a)  $\alpha = 3^\circ$ ; (b)  $\alpha = 5^\circ$ .

in these cases, too. More detailed analysis of this difference is continued in the subsequent sections.

As an interesting finding on two-dimensional unsteadiness,  $\Delta C_{l_{\text{rms}}}$  suddenly drops for NACA4806 at  $\alpha = 9^\circ$ , in the diagram of the rms fluctuation of Fig. 6. At this angle of attack, a vortex shedding pattern is altered again. Still the AFL mechanism is supposedly held with significant vortex development on the suction-side of the airfoil, Karman vortex-like alternating patterns are regained in the wake. Fig. 7 shows two of those examples. In the present simulations, we found several similar cases: NACA4806, 6606, and 6806. In these cases, shedding frequency also becomes higher.

## V. Frequency Selection Mechanism

As shown in Fig. 2, most of the present two-dimensional cases reach vortex shedding of narrow-band behavior, through either the absolute instability mechanism of wake flow, or the acoustic feedback process that involves the convective instability of the suction-side boundary layer. In Fig. 8, two such examples of spectral peaks are shown, sampled in the NACA4206 cases. In the estimation of the power spectral density throughout the present paper, the Hamming window function is applied to the time history data sampled

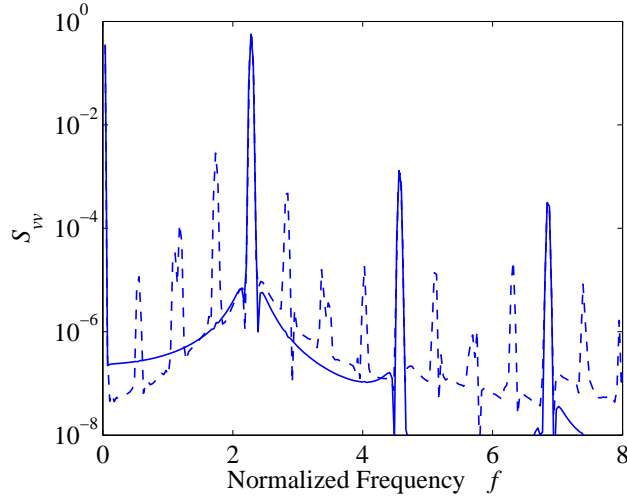


**Figure 9.** Power spectral density of NACA4206 at  $\alpha = 4^\circ$ . Dashed line is the data sampled over  $30 \leq t \leq 60$ , while solid line denotes the period  $170 \leq t \leq 200$ . Also see the caption of Fig. 8.

at normalized time interval  $\Delta t = 1.4 \times 10^{-3}$ . Most of the present cases show the behavior similar to Fig. 8: Only the primary peak of vortex shedding, and its higher harmonics are depicted, regardless of the frequency selection mechanisms, wake instability or feedback process. One of a few exceptions is the case of NACA4206 at  $\alpha = 4^\circ$ , as shown in Fig. 9; an instantaneous snap-shot was presented in Fig. 3-(a). In the spectral diagram, the two data sets are presented, sampled at different time stages. At an early stage of the simulation, the spectra clearly exhibit auxiliary peaks, approximately equally spaced,  $\Delta f \simeq 0.56$ , in addition to the primary peaks,  $f = 2.3$  and its higher harmonics, in the frequency domain. This is an indication of AFL formation as discussed in [15]. However, these auxiliary peaks gradually disappear to an almost indistinguishable level as the simulation is further continued, denoted by the solid line; the primary peaks are almost equivalent with those at the earlier stage, still showing the slight evidence of auxiliary peaks, adjacent to the primary peak. The development of vortices is clearly seen in the suction-side boundary layer in Fig. 3-(a), which implies the presence of an AFL. The primary instability mechanism that attains a discrete frequency in this case is discussed below.

When the unsteadiness is governed by the global instability due to absolute instability nature of wake velocity profile, the frequency can be predicted as saddle-point singularities of a dispersion relation in the framework of linear stability theory [e.g., 24]. For the singular point to be absolutely unstable, the imaginary part of the complex frequency  $\omega_s$  must be positive at the saddle point in the complex wave number plane. In the present study, the cusp-map method [e.g., 9, 17] is employed to identify saddle-point singularity, by applying the Rayleigh equation to a velocity-deficit profile. We also seek the most convectively unstable frequency on the velocity profiles of the suction-side boundary layer on the basis of the Orr-Sommerfeld (O-S) equation, to identify the frequency associated with an AFL, as in [25]. Similarly to the Rayleigh equation, incompressible and locally parallel base flow is assumed, extracted from the time-averaged velocity profiles along the axis normal to the wall. Then,  $N$  factor is obtained by numerically integrating the spatial growth rate solved successively, down to 90% chord, where the frequency of the most amplified disturbance is determined.

While the frequency of wake instability shows dependence on wake width, the occurrence of absolute

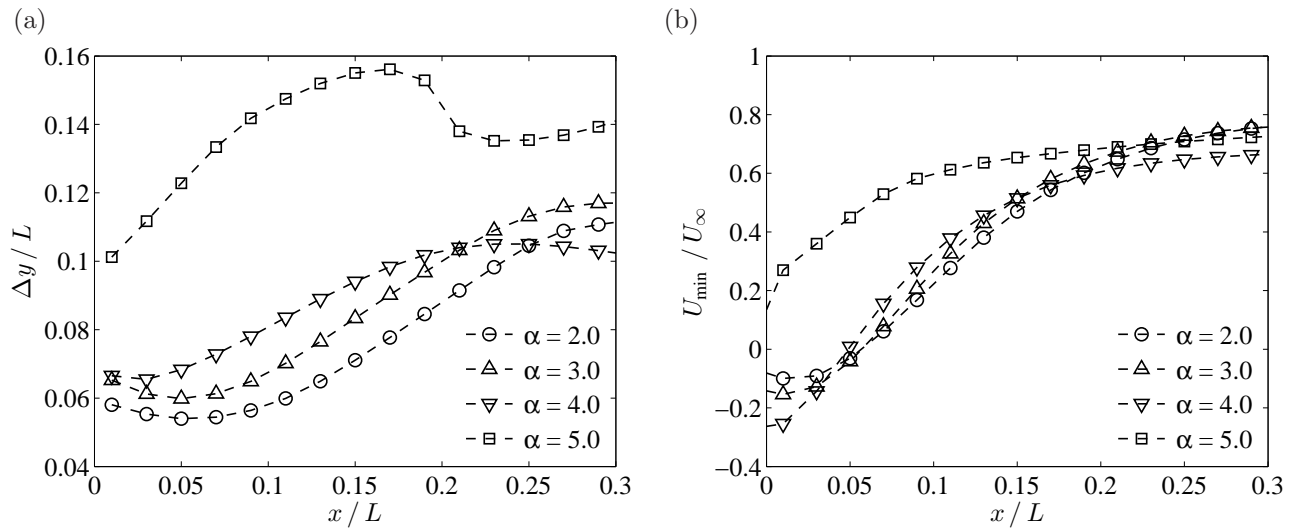


Figure 10. Comparison of wake velocity profiles of NACA4206 for  $2^\circ \leq \alpha \leq 5^\circ$ : (a) half width of velocity deficit; (b) minima of streamwise velocity.

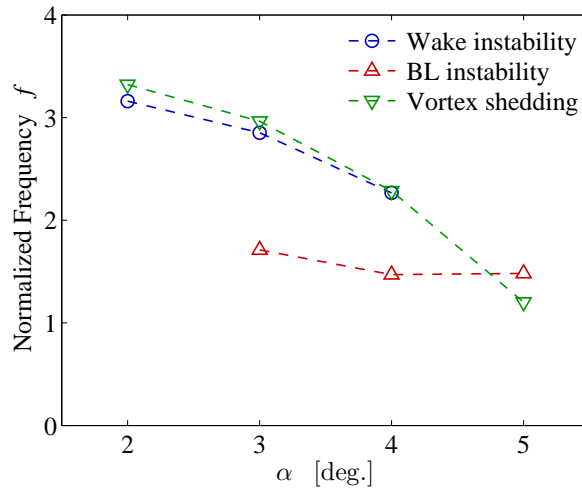
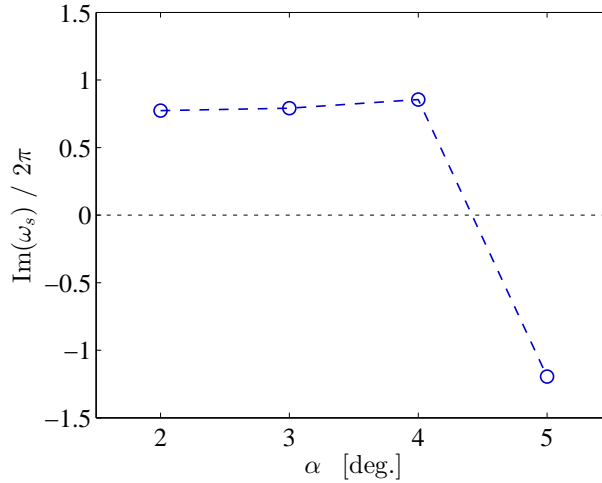


Figure 11. Comparison of absolutely unstable frequency of the wake,  $\text{Re}(\omega_s)/2\pi$  ( $\circ$ ), the most convectively amplified frequency in the suction-side boundary layer ( $\triangle$ ), and vortex shedding frequency observed in the present simulations ( $\nabla$ ) for the NACA4206 airfoil.



**Figure 12.** Imaginary part of complex singular frequencies  $\omega_s$  detected at  $x/L = 0.01$  in the NACA4206 wake. At  $\alpha = 5^\circ$ , real part of the stable singular frequency  $\text{Re}(\omega_s)/2\pi$  is 1.54.

instability greatly depends on the minimum velocity in the wake. The presence of reverse flow is more favorable for the onset of a self-induced unsteady state. Fig. 10 compares the wake velocity profiles of the NACA4206 cases for  $\alpha = 2^\circ$ – $5^\circ$ , on the streamwise distributions of half width of velocity deficit, and minimum streamwise velocity. For non-parallel, inhomogeneous wake, singular frequency shows streamwise dependence, if the Rayleigh equation is solved locally. The preceding studies on the global instability of wake flows [26, 27, 28] proposed a frequency-selection mechanism for nonlinear global modes in the spatially developing wake. That is, when the global mode grows very rapidly into its nonlinear saturation stage in the region of absolute instability and forms a steep front of the developing disturbance, the wave front at the upstream boundary may operate as a wave-maker. Then, the frequency of the global mode can be determined by the local absolute frequency at the upstream end of the absolutely unstable region: Also see the review by Chomaz [29]. In recent experimental work [30], the shedding frequency in the wake was found to be very close to the frequency predicted by this model. In the wake profiles shown in Fig. 10, the absolutely unstable region is considered to start immediately downstream from the trailing edge of the airfoil, except for the case  $\alpha = 5^\circ$ . Therefore, we examine the absolutely unstable modes for wake velocity profiles at the nearest location,  $x/L = 0.01$ , on the basis of the Rayleigh inviscid stability equation. Among the compared wakes, the case  $\alpha = 5^\circ$  shows the configuration most affected by an AFL, directly emitting vortices from the boundary layer, as shown in Fig. 3-(b). Wake width is widened significantly, and no reverse flow is present. In fact, no absolutely unstable mode is found in this velocity profile. Also, the case  $\alpha = 4^\circ$  shows a slightly different tendency from two other lower angles of attack, presumably due to the presence of a weak form of an AFL. Nevertheless, absolute instability nature appears in the three cases with reverse flow, as summarized in the following.

In Fig. 11, the frequencies determined by two linear stability analyses on wake and boundary-layer velocity profiles, and the primary vortex shedding frequencies observed in the simulations, are compared. The O-S equation was solved for the most convectively amplified frequency for the cases  $\alpha = 3^\circ$ – $5^\circ$ , while absolutely unstable frequency was found only for  $\alpha = 2^\circ$ – $4^\circ$ ; the imaginary part of the singular frequencies  $\omega_s$  are shown in Fig. 12. The frequencies of absolute instability in the present analysis agree well with the

vortex shedding frequencies at  $\alpha = 2^\circ$ – $4^\circ$ , while the most amplified frequencies on the boundary-layer velocity profile exhibit a considerable difference. Especially at  $\alpha = 4^\circ$ , in spite of several implications of an AFL, the vortex shedding frequency precisely coincides with that of the absolute instability in the near wake. On the other hand, at  $\alpha = 5^\circ$ , the vortex shedding frequency is close to the most convectively amplified frequency. Since an AFL can take only discrete frequencies [13], most amplified frequency may not necessarily coincide with the observed tonal frequency. In the present case, the frequency spacing of two adjacent AFL modes is supposedly  $\Delta f \simeq 0.56$ , from Fig. 9. Now the frequency difference at  $\alpha = 5^\circ$  is less than 0.3, which is in an acceptable range to presume the dominance of boundary-layer instability via an AFL mechanism in frequency selection.

## VI. Time-averaged Aerodynamic Forces

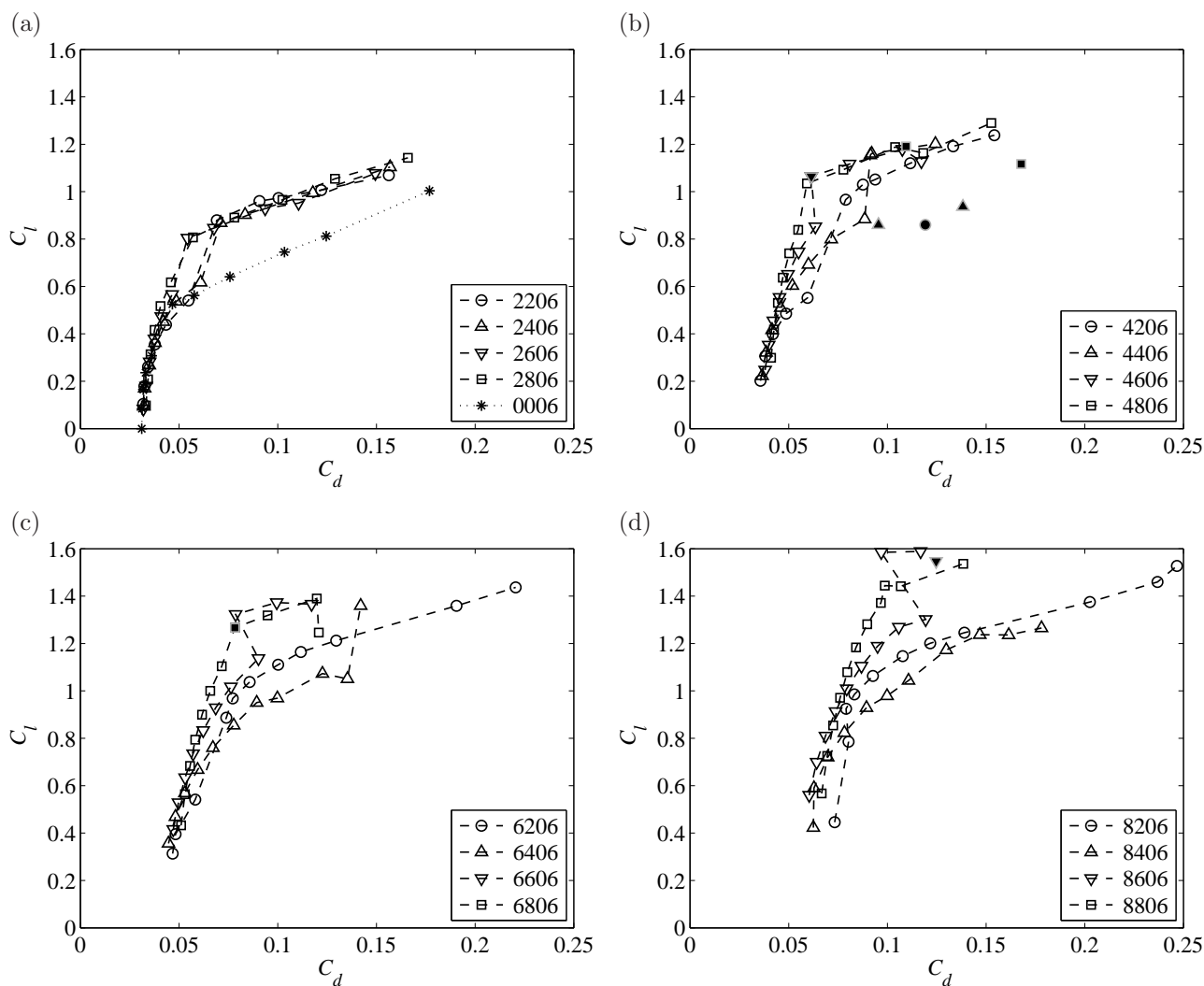


Figure 13. Lift-drag polar diagrams of (a) NACA2x06 and 0006; (b) 4x06; (c) 6x06; (d) 8x06 airfoils from  $\alpha = 0^\circ$  to  $10^\circ$ . Filled markers denote three-dimensional simulation results, shown in (b) and (d).

Here we examine the aerodynamic efficiency of the selected sets of cambered airfoils on the time average solutions. Fig. 13 shows the lift-drag polar diagrams for  $\alpha = 0^\circ$ – $10^\circ$ . In practice, low Reynolds number

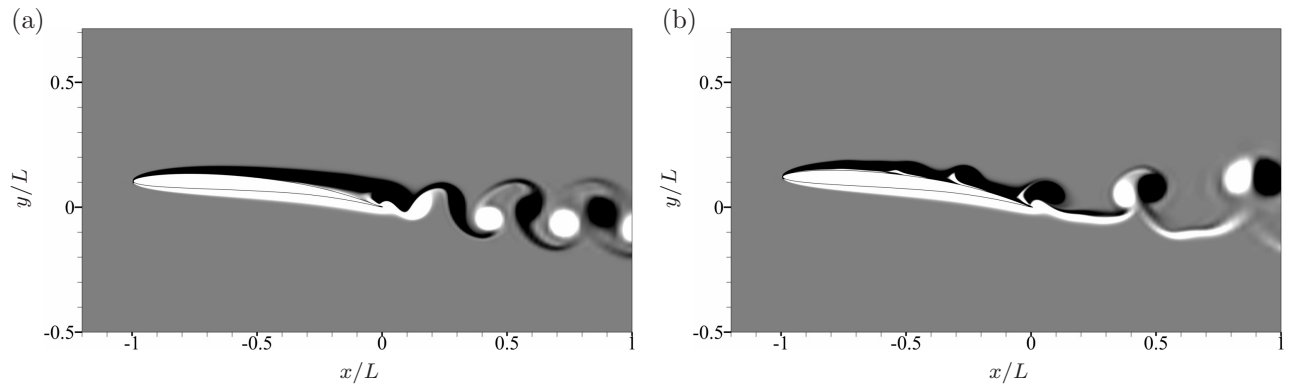


Figure 14. Instantaneous vorticity fields of NACA4606 airfoil at: (a)  $\alpha = 6^\circ$ ; (b)  $\alpha = 7^\circ$ . Also see the caption of Fig. 3.

flight in low atmospheric density would require a relatively high operational lift coefficient. For instance, a preceding study [2] suggests  $C_l = 1.5$  for a high-altitude, long-endurance flight at  $Re \sim O(10^5)$ . Although the present range of angles of attack would be insufficient for practical purpose of airfoil design, the results provide helpful information on the operational condition. The present polar diagrams cover the data points up to  $C_l \sim 1.5$ . In the present range of  $\alpha$ , an apparent stall does not arise in two-dimensional simulations. An exception is the mode of alternate vortex shedding, as illustrated in Fig. 7, in the case of NACA6806 at  $\alpha = 10^\circ$ , where a sharp drop of  $C_l$  is seen in Fig. 13-(c). In three-dimensional results, however, NACA4806 shows a slight decrement of lift, while drag significantly increases, between  $\alpha = 8^\circ$  and  $10^\circ$ . This can be considered as a stall at low Reynolds number.

As for the effect of camber height on the aerodynamic force, the increase of camber height leads to higher  $C_d$ , but it also increases attainable  $C_l$ , seen in the drag polar of Fig. 13. On the effect of maximum camber location, the aft cambered airfoil generally shows favorable features at low Reynolds number, as was reported in other studies [31, 20]. The aft camber reduces the size of a trailing-edge separation region at moderate  $\alpha$ , which effectively increases lift while suppressing drag. The most aft cambered airfoils, NACAx806 show a better aerodynamic performance, attaining higher lift-to-drag ratios at  $\alpha \sim 5^\circ$ , compared with other families of airfoils. By further increasing  $\alpha$ , however, NACAx606 airfoils achieve better lift-to-drag ratios at some operating points. Especially, drag even reduces in NACA4606 at  $\alpha = 7^\circ$ , 6606 at  $\alpha = 8^\circ$ , and 8606 at  $\alpha = 9^\circ$ , from the states at smaller  $\alpha$ . These operating points correspond to the onset of an AFL, altering vortex shedding patterns. The change of flow motions of NACA4606 is shown in Fig. 14. The AFL onset conditions of NACAx606 airfoils also correspond to their maximum lift-to-drag ratios,  $L/D = 15\text{--}17$ .

The transition of vortex shedding patterns due to the onset of an AFL, is well related with the difference of hydrodynamic instability mechanisms between wake and boundary layer [17]. Fig. 15 shows the change of separation regions, and associated surface pressure distributions of the time-averaged fields of NACA4606 shown in Fig. 14. At  $\alpha = 6^\circ$ , the upper-side boundary layer separates at about 60% chord location which corresponds to the maximum camber location, and forms a trailing-edge separation bubble of nearly dead-fluid motion, which leads to a flat pressure distribution. On the other hand, at  $\alpha = 7^\circ$ , the boundary layer separates almost at the leading edge, and reattaches at 60% chord, forming a very thin separation bubble. The presence of reverse flow prompts Rayleigh's inviscid instability. Especially, a separation bubble behind the leading edge increases the receptivity of external disturbances. Introduced via an acoustic feedback process at the leading edge, hydrodynamic instability waves develop into discernible vortical motions, shed

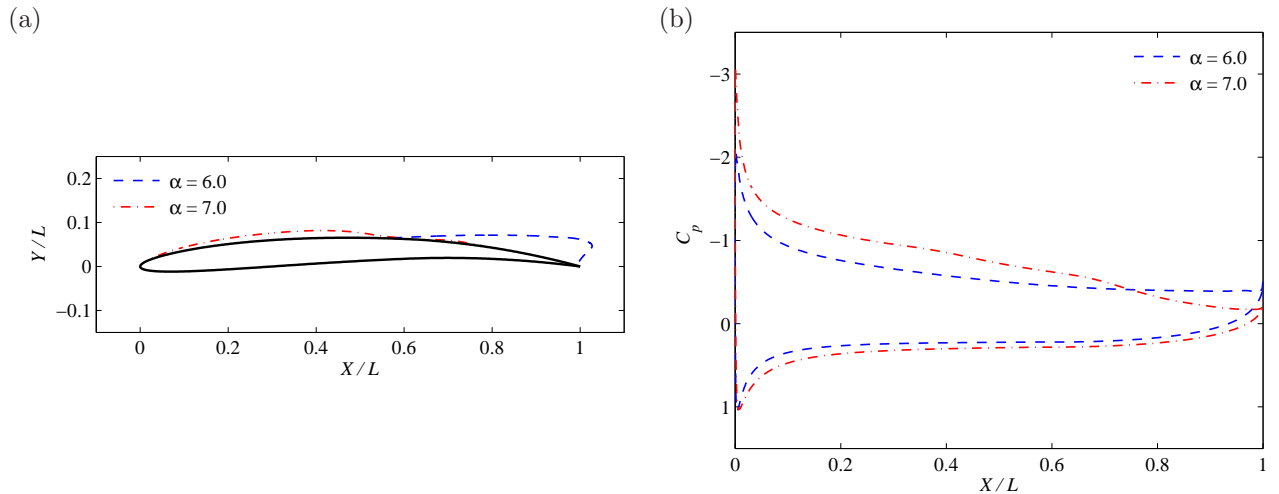


Figure 15. Difference in time-averaged flow field of NACA4406 at  $\alpha = 6^\circ$  and  $7^\circ$ : (a) separation bubbles around the airfoil; (b) time-averaged pressure coefficient.

into the wake. These two-dimensional vortices prevent trailing-edge separation, which significantly increases the lift force. The attached boundary layer shows relatively steep pressure recovery toward the trailing edge; this resembles the “separation ramp” concept as in [2], originally proposed to control the size of a trailing-edge separation region. In the present case, however, it is attained by a leading-edge separation bubble, and a subsequent, attached boundary layer near the trailing edge.

To examine the validity of aerodynamic properties evaluated in two dimensions, three-dimensional results should be referenced, especially when an AFL formation alters aerodynamic forces. NACA4606 and NACA6806 airfoils both form an AFL at  $\alpha = 7^\circ$ , attaining maximum  $L/D$ . They were examined in three dimensions, but resulted in two-dimensional time-periodic states. Since an AFL can be explained with a two-dimensional mechanism [12, 17], the two-dimensional unsteady phenomenon can be dominant unless a separated shear layer on suction side becomes sufficiently unstable. The other three airfoils of the NACA4x06 set, all reached self-sustaining, three-dimensional unsteady states at  $\alpha = 8^\circ$ . While the aft cambered airfoil, NACA4806 attains the time-averaged lift and drag close to its two-dimensional solution, the other two forward cambered airfoils result in an apparent decrease of lift. Another aft cambered airfoil, NACA8606 also realized aerodynamic forces close to those of the two-dimensional result at  $\alpha = 10^\circ$  in three dimensions; the achieved lift coefficient, higher than 1.5, is about the maximum in the present parametric study. In the rest of this section, we would discuss the difference of the results obtained in two and three dimensions, respectively, by looking into the solutions of NACA4406 and 4806, relatively forward, and aft cambered airfoils at  $\alpha = 8^\circ$ .

Figs. 16 and 17 compare the instantaneous vortex shedding patterns of each airfoil, in two and three dimensions. Two-dimensional flows are both somewhat similar on the development of vortices in the boundary layer, forming an AFL. The vortex pairs are closely coupled, shed into the wake. However, their three-dimensional solutions are rather different. In the NACA4406 case, the vortical motions calm down on the suction side except near the trailing edge, in the three-dimensional snapshot. A larger separation bubble arises on the aft part of the airfoil, leading to a trailing-edge stall. Vortices shed in the wake gradually break down associated with the development of spanwise fluctuations. The three-dimensional result of NACA4206

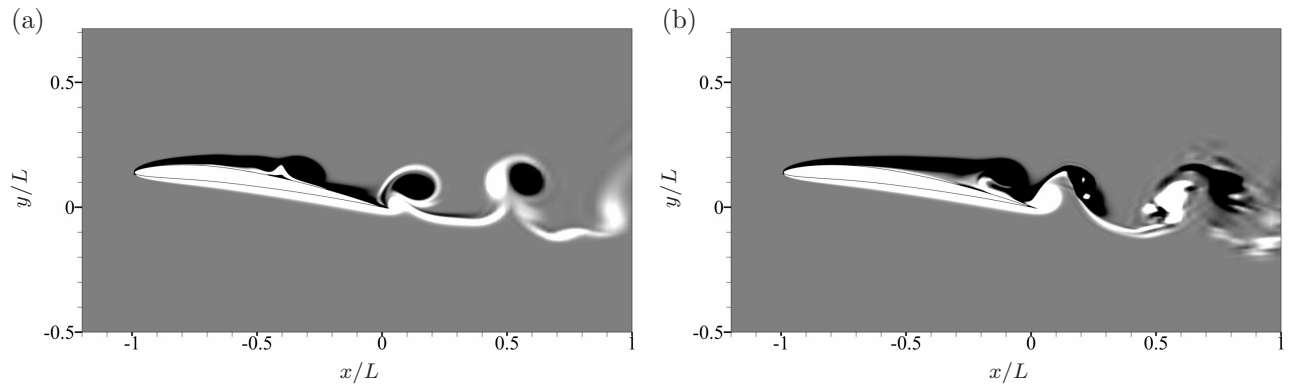


Figure 16. Instantaneous vorticity fields of NACA4406 airfoil at  $\alpha = 8^\circ$  obtained in two dimensions (*left*) and in three dimensions on an  $x$ - $y$  view (*right*). Also see the caption of Fig. 3.

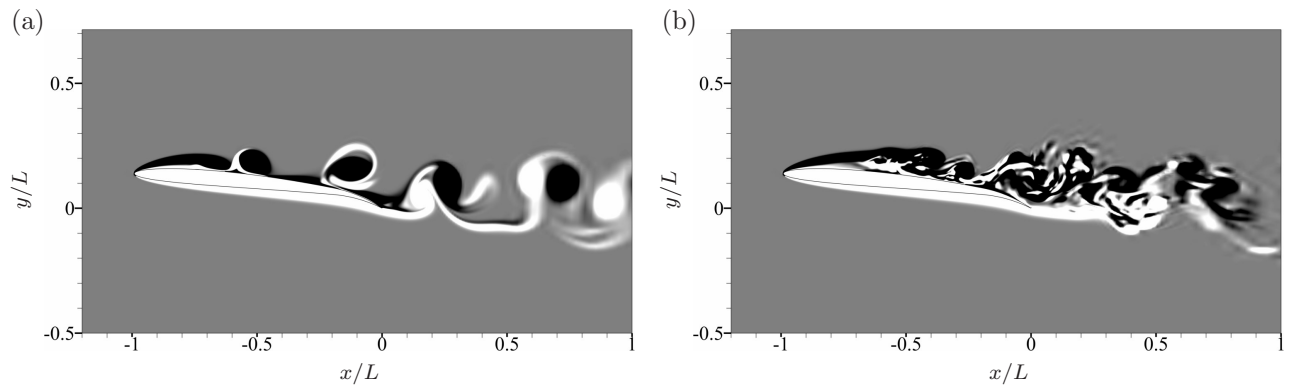


Figure 17. Instantaneous vorticity fields of NACA4806 airfoil at  $\alpha = 8^\circ$  obtained in two dimensions (*left*) and three dimensions on an  $x$ - $y$  view (*right*). Also see the caption of Fig. 3.

airfoil has many similarities with the present case. It also exhibits a large separation bubble at the trailing edge, and reduces lift from its two-dimensional result. On the other hand, in the NACA4806 case, rather complex vortex structures arise on the suction side behind the laminar shear layer at the leading edge. The boundary layer does not seem fully turbulent; it is rather transitional. However, due to the sufficient complexity of three-dimensional eddies, the transitional boundary layer induces reattachment in the middle, and stays attached thereafter. This can be regarded as the extension of the laminar separation bubble, usually supposed to arise at higher Reynolds number.

Fig. 18 directly compares the separation bubbles that form on the suction side of the two airfoils, depicted on the time-averaged velocity fields, in both two and three-dimensional simulations. It is interesting that the separation point of NACA4406 is modified from the leading edge in the two-dimensional result, to about 30% chord in three dimensions. In contrast, NACA4806 shows a separation shear layer clearly at the leading edge. Although the resultant separation bubble is more elongated in the three-dimensional case, the transitional boundary layer prompts reattachment, which prevents the severe reduction of lift force. The pressure distributions in Fig. 19 are also consistent with the observations above. The lift-force drop of NACA4406 in three dimensions is primarily due to the flat pressure profile on the separation bubble. All other cases show relatively flat  $C_p$  on the leading-edge separation bubble; then pressure recovery is achieved toward the trailing edge, as was shown in Fig. 15.

As observed in the present cases with AFL formation, the presence of a leading-edge separation bubble can drastically improve aerodynamic performance. An attached boundary layer that prevails behind a separation

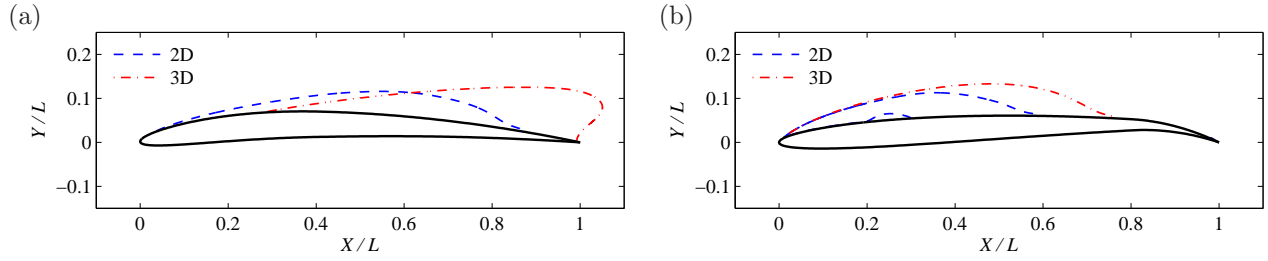


Figure 18. Comparison of separation bubbles in two and three dimensions at  $\alpha = 8^\circ$  for: (a) NACA4406; (b) NACA4806.

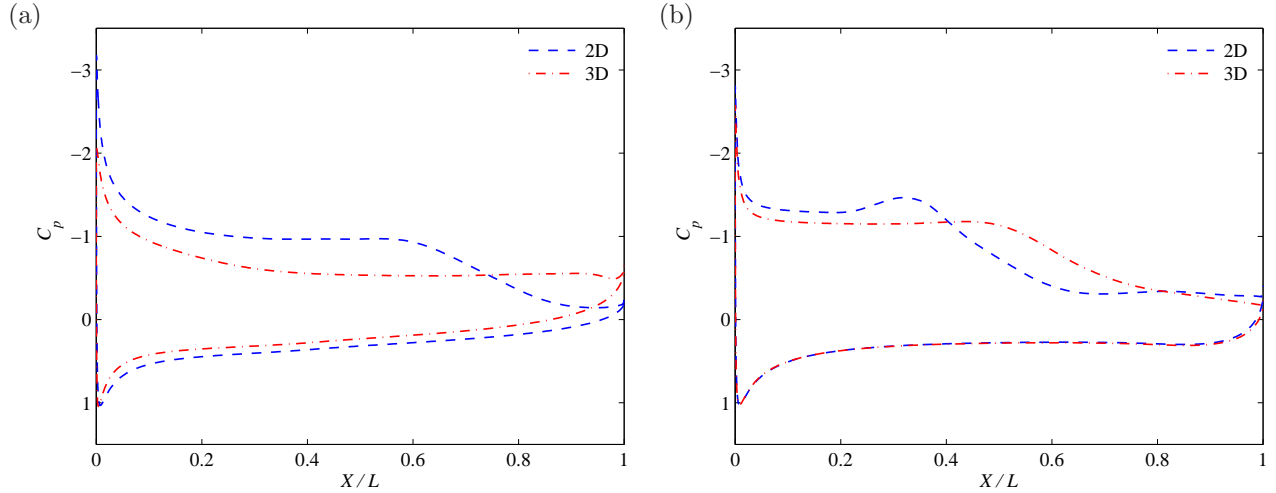
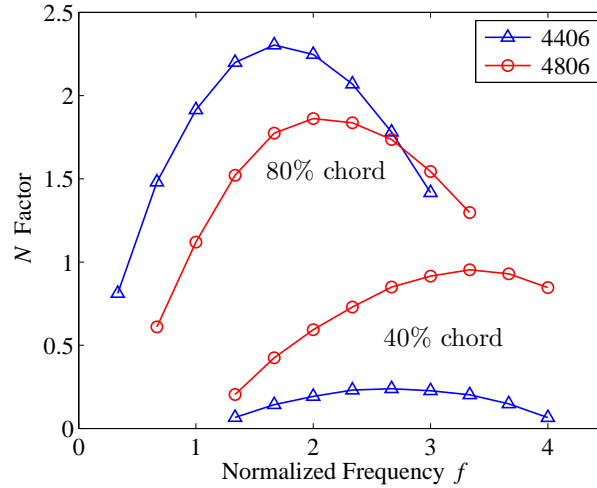


Figure 19. Comparison of surface pressure distributions in two and three dimensions at  $\alpha = 8^\circ$  for: (a) NACA4406; (b) NACA4806.

bubble, attains a greater pressure recovery for lift increments. In the literature, however, the critical Reynolds number is estimated as 50,000–70,000 for the occurrence of reattachment, to form a laminar separation bubble [1, 8]. The present Reynolds number is even lower than the critical bound. This is presumably due to the presence of a non-negligible acoustic disturbance in the numerical simulations at a moderate Mach number. Since the sound pressure of two-dimensional acoustic scattering shows  $M^{1/2}$  dependence, its velocity component obeys the dependence of  $M^{3/2}$ , in addition to the amplification of dynamic pressure. Usually, experimental studies of a low-Reynolds-number airfoil must be conducted at very low Mach number, in laboratory environments at ground level. However, the magnitude of acoustic disturbances fed back into a boundary layer grows very rapidly as the inflow Mach number increases, which may cause reattachment via the development of an AFL, at the Reynolds number quite lower than 50,000. In the numerical study conducted at  $Re = 2.3 \times 10^4$  and  $M = 0.2$  [5], boundary-layer reattachment also occurs on an NACA0012 airfoil at  $\alpha = 6^\circ$ , which contradicts the experimental observation referenced in their paper.

The significant difference of aerodynamic performance between NACA4406 and 4806 airfoils in three-dimensional results can be explained from the view point of hydrodynamic instability of suction-side boundary layers. The convex surface behind the leading edge would relax adverse pressure gradient, and associated



**Figure 20.** Frequency dependence of  $N$  factor at 40 percent and 80 percent chord locations integrated from the leading edge for NACA4406 and 4806 at  $\alpha = 6^\circ$ .

velocity profile, which stabilizes the shear layer. The leading-edge separation bubble of NACA4806 in Fig. 18 clearly indicates the augmented receptivity in the neighborhood. Again, we would conduct a linear stability analysis on the O-S equation to clarify the frequency dependence of the suction-side shear layer instability. However, the development of velocity fluctuations in the three-dimensional cases is highly non-linear, which may invalidate the present linear analysis. Besides, the substantial reverse flow past the boundary-layer separation destabilizes the iterative approach to solve for an eigenvalue of the O-S equation. Alternatively, a more direct sensitivity study based on the forced Navier-Stokes equations, employed in [9, 16], would be effective in these circumstances. Instead, we choose the flow field at relatively lower angle of attack,  $\alpha = 6^\circ$ , where no leading-edge separation occurs in both cases, to ensure the solution of the O-S equation. Here, time-averaged, two-dimensional solutions are employed as base flow.

Fig. 20 compares the frequency dependence of  $N$  factor, integrated to 40% chord, and 80% chord locations for both NACA4406 and 4806 airfoils. Since NACA4406 holds a relatively large separation bubble at the trailing edge, the maximum value of  $N$  factor is larger than that of NACA4806, when integrated throughly to the trailing edge. However, down only to 40% chord, NACA4806 shows even greater  $N$  factor, especially in a higher frequency range, due to the strong adverse pressure gradient at the leading edge. It can be inferred that the convex upper surface on the front part of the chord should lower the growth rate of hydrodynamic disturbances. The chordwise maximum  $N$  factor, shown in Fig. 21, is also consistent with the present hypothesis. Fig. 22 presents the chordwise growth of rms tangential velocity fluctuation in logarithmic scale at  $\alpha = 8^\circ$ . Due to the augmented instability by the presence of a leading-edge separation bubble in the three-dimensional simulation, the magnitude of fluctuation in the NACA4806 case is even prominent in growth rate, and quickly reaches a non-linear level toward the middle of the chord. On the other hand, the NACA4406 airfoil shows even moderate growth throughout the boundary layer, slightly exceeding the fluctuation of NACA4806 near the trailing edge. The observation indicates that the forward cambered airfoils, such as NACA4206 and NACA4406, delay boundary-layer transition due to the suppression of instability growth near a leading edge. Rather, the relatively flat profile behind a leading edge stimulates the development of small eddies, which induces the reattachment to form a laminar separation bubble. Eventually, the present

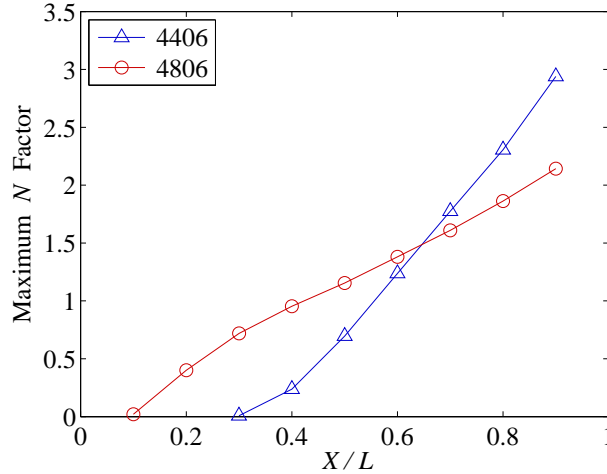


Figure 21. Chordwise growth of maximum  $N$  factor at each  $X$  location for NACA4406 and 4806 at  $\alpha = 6^\circ$ .

aft cambered airfoil can attain better aerodynamic performance, especially at moderate to relatively high angles of attack.

## VII. Acoustic Feedback Loop in Three-dimensional Fields

The overestimate of lift force in several two-dimensional cases was investigated in comparison with three-dimensional fields in the previous section. While some cases maintain two-dimensionality with an AFL that holds off bulk separation, three-dimensional cases either successfully develop a transitional boundary layer with a laminar separation bubble, or suffer a trailing-edge stall to lose lift. On the other hand, an AFL with tonal noise generation is essentially a two-dimensional mechanism. The phase variation in the spanwise direction, such as the development of three-dimensional eddies, would reduce the intensity of tonal noise [11]. To form the resonance between hydrodynamic instability waves and acoustic disturbances scattered at a trailing edge, a strong correlation in the spanwise direction is supposedly required. In this section, we investigate the difference of the three-dimensionality observed in the aforementioned two cases, NACA4406 and 4806 airfoils at  $\alpha = 8^\circ$ , focusing on the tone noise generation and its relevance with an AFL mechanism.

Fig. 23 compares the instantaneous vortical structures in the suction-side boundary layer of each airfoil. In both the cases, spanwise vortical motions develop in the shear layer separated at the leading edge. These vortices are hydrodynamic instability waves reproduced in three dimensions, induced through the acoustic feedback process, occurring near the leading edge. As inviscid, inflection-point instability is held by the separated shear layer, these hydrodynamic disturbances quickly grow in magnitude, which resembles Kelvin-Helmholtz instability. While the NACA4406 case retains the quasi two-dimensional vortices down to 60–70% of the chord, they abruptly break down and merge into a longitudinal vortical structure that develops from the middle of the chord. On the other hand, longitudinal vortices arise closer to the leading edge, as spanwise vortices disappear, in the NACA4806 case. Still large-scale spanwise coherence can be recognized in the figure. It will be discussed quantitatively below.

Fig. 24 visualizes the rms spanwise velocity fluctuation  $w'_{\text{rms}}$ , induced by the longitudinal vortical motions. The difference between the two airfoils is recognized very clearly. In the NACA4406 case, the maximum of

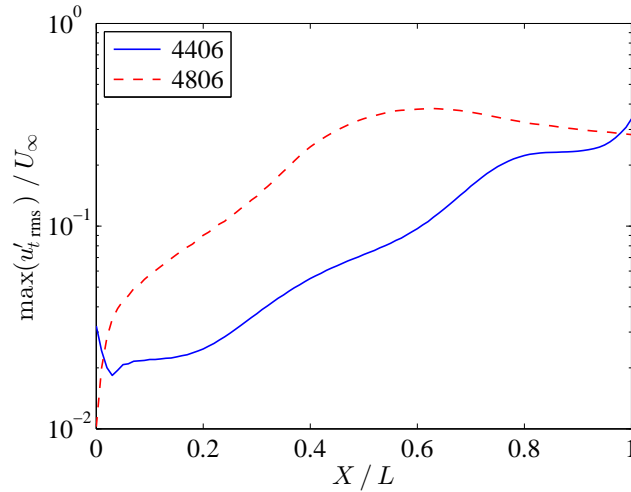


Figure 22. Chordwise growth of maximum magnitude of rms tangential velocity fluctuation  $u'_{t,rms}$  for NACA4406 and 4806 at  $\alpha = 8^\circ$ .

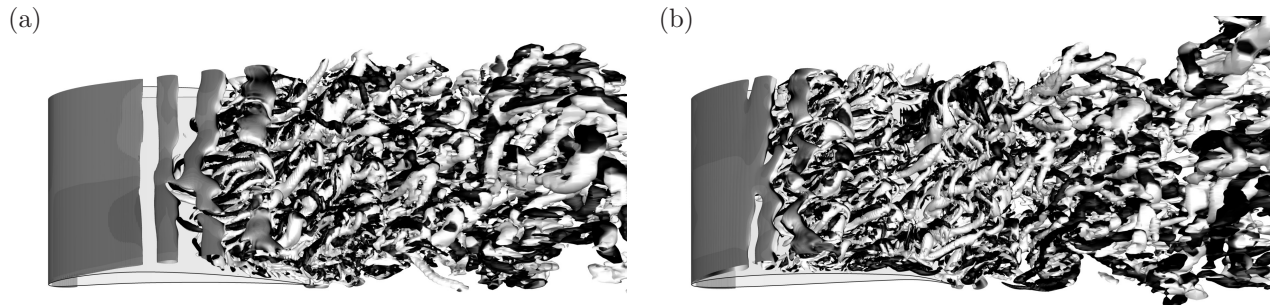


Figure 23. Visualization of instantaneous Q-vortex isosurfaces at  $Q = 10(U_\infty/L)^2$  colored by streamwise vorticity  $\omega_x L/U_\infty$  ranging between  $-1$  and  $+1$  from black to white for (a) NACA4406 and (b) NACA4806 at  $\alpha = 8^\circ$ .

$w'_{rms}$  occurs in the wake near the trailing edge, probably due to vortex shedding therefrom. In the NACA4806 case, however, a considerable spanwise fluctuation is observed over the upper surface, from the middle of the leading-edge separation bubble to the wake, which corresponds to the transitional behavior captured in Fig. 23. This resembles the laminar-turbulent transition that arises past laminar separation at moderate Reynolds numbers [6, 3, 7], although the present Reynolds number is even lower.

In the present simulations, sufficiently three-dimensional flow is achieved in the suction-side boundary layer of NACA4806, while more laminar-flow features are retained in the NACA4406 case. Fig. 25 shows the spanwise auto-correlation of flow variables  $u$ ,  $v$ , and  $p$ , sampled at the 10% chord location on the suction-side wall, and in the region of very active vortex shedding,  $0.1L$  above the trailing edge. At 10% chord, where flow is mostly laminar, pressure fluctuations are well correlated in both the cases. Especially, the NACA4406 case seems practically two-dimensional. It is also consistent with the spanwise vortical structures past the leading edge, presented in Fig. 23.

Just above the trailing edge where eddies are shed into the wake, the spanwise correlation is somewhat weakened, depending on the complexity of three-dimensional motions. In both the cases, the streamwise

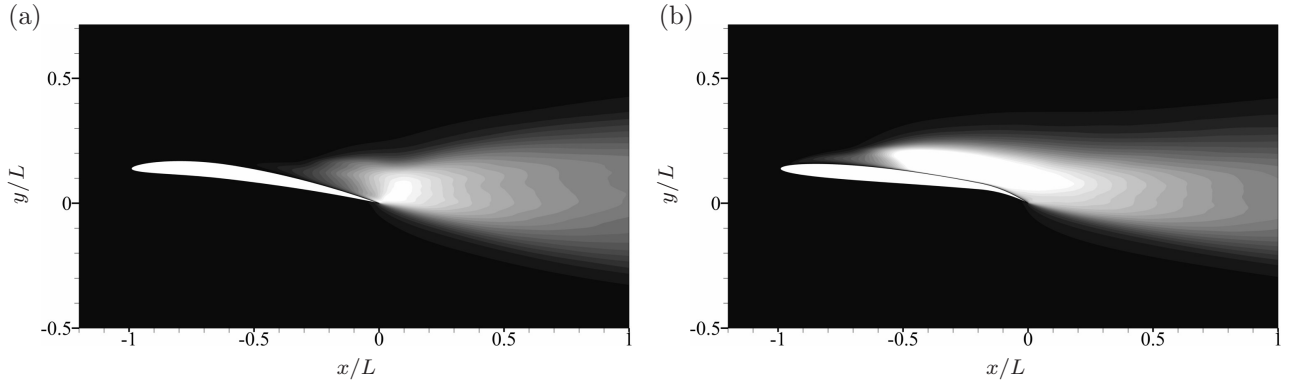


Figure 24. Two-dimensional contours of rms spanwise velocity fluctuation  $w'_{\text{rms}}$  for (a) NACA4406 and (b) NACA4806 at  $\alpha = 8^\circ$ . Gray scale ranges between 0 and  $0.2U_\infty$  from black to white.

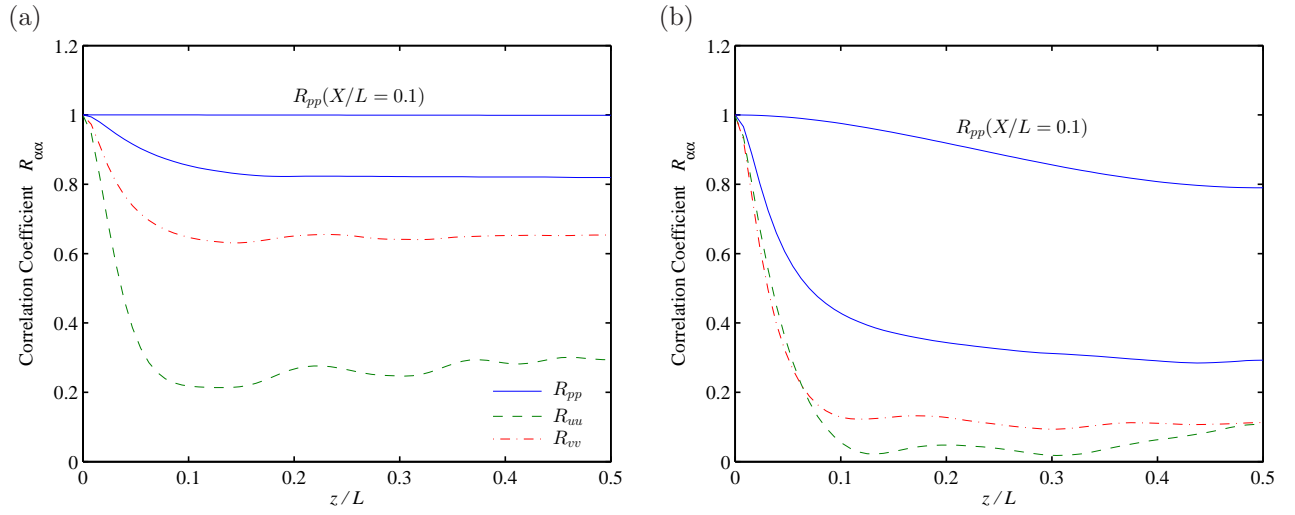


Figure 25. Spanwise auto-correlation coefficients  $R_{pp}$ ,  $R_{uu}$  and  $R_{vv}$ , at  $0.1L$  above the trailing edge, and  $R_{pp}$  on the suction side of the airfoil at  $X/L = 0.1$  for (a) NACA4406 and (b) NACA4806 at  $\alpha = 8^\circ$ .

velocity fluctuation  $u$  is the most uncorrelated. However, the other quantities,  $v$ , and rather  $p$ , are more correlated. This can be interpreted as the spanwise phase alignment due to two-dimensional noise emission from the trailing edge. The normal velocity  $v$  represents a dipole-sound scattering at the trailing edge, in addition to the hydrodynamic disturbances. Pressure fluctuation  $p$  is also composed of acoustic and hydrodynamic components. In the present case, relatively correlated pressure would be responsible for the two-dimensional mechanism of an AFL. Although, three-dimensional eddies affect the AFL process, the primary component of the AFL retains two-dimensionality. This also explains the well-correlated pressure distribution in the laminar region near the leading edge. The acoustic feedback process of primary tones should be two-dimensional.

Fig. 26 shows the spectra of pressure fluctuation sampled at  $0.5L$  above the trailing edge. As shown in Figs. 16 and 17, hydrodynamic motions only exist sufficiently below the sampling location. Therefore, the spectra should mostly represent the sound pressure scattered from the airfoil surface. Time-history data sets were sampled over 30 non-dimensional time in both cases. Besides, spectral data were averaged at five different, equally spaced spanwise locations. Although the flow field of NACA4806 shows rather transitional features, both the cases clearly exhibit narrowband peaks,  $f = 1.56$  for NACA4406 and  $f = 1.23$

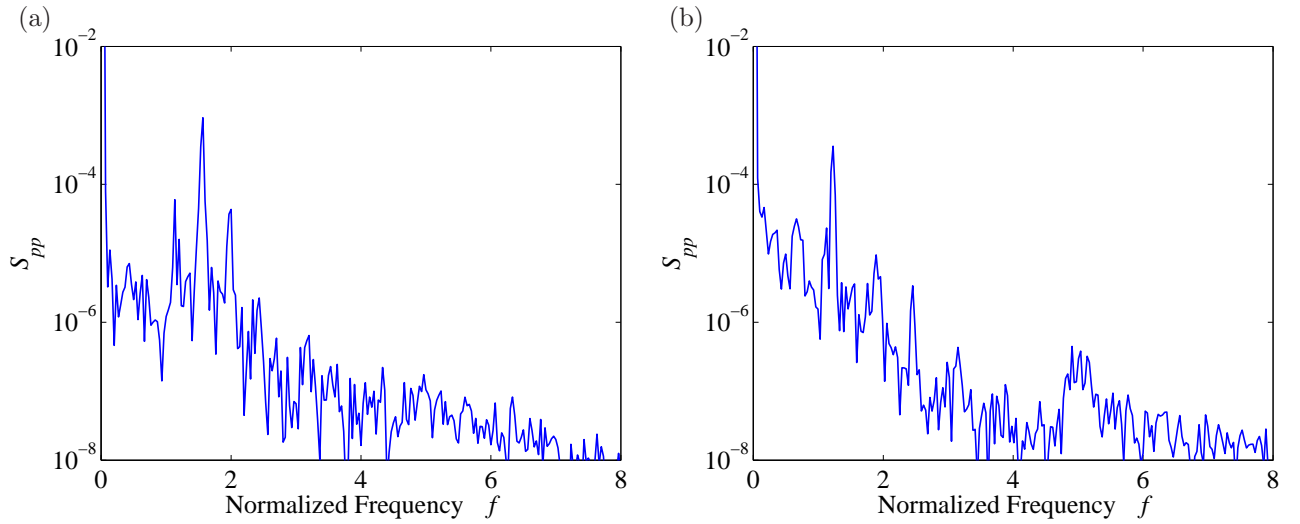


Figure 26. Power spectral density of pressure  $S_{pp}$ , sampled at  $0.5L$  above the trailing edge for (a) NACA4406 and (b) NACA4806 at  $\alpha = 8^\circ$ .

for NACA4806, respectively, normalized by  $U_\infty$  and  $L$ . At this angle of attack, the vortex shedding of two-dimensional results may become temporally non-periodic. Shedding patterns vary intermittently, resulting in a relatively broadband nature. On the other hand, when sampled near the leading edge in a laminar boundary layer in the three-dimensional cases, the same peak frequencies are also obtained. They correspond to the primary frequencies of instability waves, which implies the presence of an AFL in these three-dimensional simulations.

Especially, the more laminarized case of NACA4406 clearly shows secondary tones as well, adjacent to the primary one as in Fig. 26-(a). The frequency differences  $\Delta f$  from the primary tone are both 0.42. If these spectra can be considered as discrete modes observed in an AFL,  $\Delta f$  can be given as [12, 13]:

$$\Delta f = \frac{1}{d} \left( \frac{1}{U_c} + \frac{1}{c - U_\infty} \right)^{-1} \quad (1)$$

where  $c$  is sound speed,  $U_c$  is the phase velocity of instability waves, and  $d$  is the distance between the trailing edge and the chord location where hydrodynamic wave that forms feedback resonance, is initiated by an acoustic feedback mechanism; in the present case,  $d = L$ , if acoustic wave is assumingly fed back at the leading edge. By using Eq. (1),  $\Delta f = 0.42$  corresponds to  $U_c \simeq 0.47U_\infty$ , which is a little higher than  $U_c/U_\infty \simeq 0.4$  reported in [14] and also usually given by a linear stability analysis, but still in a reasonable range; the phase velocity  $U_c \simeq 0.5U_\infty$  was reported in the two-dimensional calculation of NACA0006 airfoil at  $Re = 20,000$  [17]. The present observation strongly suggests the formation of a feedback loop mechanism.

On the other hand, in the NACA4806 case Fig. 26-(b), very weak secondary peaks are detected in the continuous spectrum at  $f = 0.66$  and  $1.89$  near the primary peak  $f = 1.23$ . The frequency difference from the primary peak is  $\Delta f = 0.57$  and  $0.66$ , respectively. If we adopt  $\Delta f = 0.66$  for Eq. (1) in this case, the phase velocity must be increased up to  $U_c \simeq 0.8U_\infty$ , twice as large as that usually predicted by the linear stability analysis. The phase velocity seems a little too large; however, it is yet possible because of highly non-linear hydrodynamic growth in the suction-side boundary layer, in the NACA4806 case, as shown in Fig. 22. Alternatively, it is also possible that the feedback process critical to form a resonant loop, may occur somewhere in the chord, other than at the leading edge, which reduces  $d$  in Eq. (1) to allow an additional

increment in  $\Delta f$ . For instance, at 20-30% chord, noticeable vortical structure begins to develop abruptly in the separation bubble, as shown in Fig. 23-(b). This could be the indication of hydrodynamic modes excited directly by acoustic disturbance.

In summary, as three-dimensional eddies develop in the separation shear layer, the magnitude of sound emission should be lowered. Two-dimensional calculations may overestimate the resonance level of an AFL that hydrodynamically stimulates a suction-side boundary layer, by inducing strong vortical motions that would force reattachment in the middle of the chord. Despite the NACA4806 case that successfully introduces a laminar separation bubble, the three-dimensionality added to the boundary layer may prohibit reattachment on the suction side, which decreases lift. Besides, forward cambered airfoils such as NACA4406 would stabilize the boundary layer by delaying pressure recovery in the shear layer past the leading edge. This is consistent with delayed separation of NACA4406 in three-dimensional case as shown in Fig. 18, which laminarizes leading-edge neighborhood. It is also confirmed in the linear stability analysis that shows the reduction in the growth rate of hydrodynamic disturbances, especially in a higher frequency range, near the leading edge for forward camber.

## VIII. Conclusions

The aerodynamic characteristics of low-Reynolds-number airfoils can be altered drastically, due to the hydrodynamic effect of an AFL that arises at moderate Mach number. In fixed flow conditions  $Re = 10^4$  and  $M = 0.2$ , the present numerical study of NACA four-digit airfoils shows that the acoustic disturbances of airfoil self-noise significantly change unsteady flow states, by forming an AFL associated with hydrodynamic instability mechanisms. With the presence of an AFL, two-dimensional instability waves develop into discernible vortices on the suction side of the airfoil. Consequently, the size of a separation bubble located at the trailing edge reduces, which leads to lift gain. By increasing an angle of attack, the unsteady motion in the suction-side boundary layer is more intensified. This may cause boundary-layer reattachment in the middle of the chord, whereas the separation occurs more upstream. The resultant time-averaged flow field has similarities with a laminar separation bubble that induces laminar-turbulent transition, observed at moderate Reynolds numbers, but presumably higher than the present case. The magnitude of hydrodynamic instability waves excited via an AFL becomes very significant as Mach number increases, which prompts reattachment at the Reynolds number considerably lower than the critical bound reported in the literature, about  $5 \times 10^4$  [1, 8].

The effect of maximum camber locations is examined in both time-averaged aerodynamic force and unsteady characteristics. In terms of aerodynamic performance, the aft camber achieves higher lift force at higher  $L/D$ , evaluated in the present unsteady simulations, consistent with other experimental and numerical studies [31, 20]. Unless an AFL arises, the aft camber reduces the size of a trailing-edge separation bubble, which delays pressure recovery to achieve higher lift. In addition, the onset of an AFL rather works well with the aft cambered airfoils to further improve aerodynamic performance. As captured in three-dimensional visualization, a transitional boundary layer is provoked by two-dimensional disturbances fed back at the leading edge, developing longitudinal eddies with spanwise motions, which prevents bulk separation. On the other hand, the forward camber reduces the adverse pressure gradient near the leading edge, decreasing the growth rate of instability waves in a separation shear layer. Although the results of two-dimensional computations may present flow reattachment on the suction side, due to strong resonance of

a two-dimensional AFL mechanism, the spanwise fluctuations in three-dimensional simulations also weaken the resonance of an AFL. Because of these, the forward cambered airfoils tend to facilitate a trailing-edge stall, which significantly lowers the aerodynamic performance.

This work was supported by Grant-in-Aid for Scientific Research (C) from Japan Society for the Promotion of Science (Grant No. 25420139). Computational resources were provided by JAXA Supercomputer System.

## References

- [1] Lissaman, P. B. S., “Low-Reynolds-number airfoils,” *Ann. Rev. Fluid Mech.*, Vol. 15, 1983, pp. 223–239.
- [2] Maughmer, M. D. and Somers, D. M., “Design and experimental results for a high-altitude, long-endurance airfoil,” *J. Aircraft*, Vol. 26, No. 2, 1989, pp. 148–153.
- [3] Liebeck, R. H., “Laminar separation bubbles and airfoil design at low Reynolds numbers,” *AIAA Paper 1992-2735*, 1992.
- [4] Anyoji, M., Nose, K., Ida, S., Numata, D., Nagai, H., and Asai, K., “Aerodynamic measurements in the Mars Wind Tunnel at Tohoku University,” *AIAA Paper 2011-0852*, 2011.
- [5] Kojima, R., Nonomura, T., Oyama, A., and Fujii, K., “Large-eddy simulation of low-Reynolds-number flow over thick and thin NACA airfoils,” *J. Aircraft*, Vol. 50, No. 1, 2013, pp. 187–196.
- [6] Roberts, W. B., “Calculation of laminar separation bubbles and their effect on airfoil performance,” *AIAA J.*, Vol. 18, No. 1, 1980, pp. 25–31.
- [7] Lian, Y. and Shyy, W., “Laminar-turbulent transition of a low Reynolds number rigid or flexible airfoil,” *AIAA J.*, Vol. 45, 2007, pp. 1501–1513.
- [8] Shyy, W., *Aerodynamics of low Reynolds number flyers*, Cambridge university press, 2008.
- [9] Jones, L. E., Sandberg, R. D., and Sandham, N. D., “Stability and receptivity characteristics of a laminar separation bubble on an aerofoil,” *J. Fluid Mech.*, Vol. 648, 2010, pp. 257–296.
- [10] Ikeda, T. and Atobe, T., “Numerical studies of acoustic effects on 2D airfoil aerodynamics at a low Reynolds number,” *AIAA Paper 2012-0700*, 2012.
- [11] Paterson, R. W., Vogt, P. G., Fink, M. R., and Munch, C. L., “Vortex noise of isolated airfoils,” *J. Aircraft*, Vol. 10, No. 5, 1973, pp. 296–302.
- [12] Longhouse, R. E., “Vortex shedding noise of low tip speed, axial flow fans,” *J. Sound Vib.*, Vol. 53, No. 1, 1977, pp. 25–46.
- [13] Arbey, H. and Bataille, J., “Noise generated by airfoil profiles placed in a uniform laminar flow,” *J. Fluid Mech.*, Vol. 134, 1983, pp. 33–47.
- [14] Nash, E. C., Lowson, M. V., and McAlpine, A., “Boundary-layer instability noise on aerofoils,” *J. Fluid Mech.*, Vol. 382, 1999, pp. 27–61.

- [15] Desquesnes, G., Terracol, M., and Sagaut, P., “Numerical investigation of the tone noise mechanism over laminar airfoils,” *J. Fluid Mech.*, Vol. 591, 2007, pp. 155–182.
- [16] Jones, L. E. and Sandberg, R. D., “Numerical investigation of tonal airfoil self-noise generated by an acoustic feedback-loop,” *J. Sound Vib.*, Vol. 330, No. 25, 2011, pp. 6137–6152.
- [17] Ikeda, T., Atobe, T., and Takagi, S., “Direct simulations of trailing-edge noise generation from two-dimensional airfoils at low Reynolds numbers,” *J. Sound Vib.*, Vol. 331, No. 3, 2012, pp. 556–574.
- [18] Inasawa, A., Ninomiya, C., and Asai, M., “Suppression of tonal trailing-edge noise from an airfoil using a plasma actuator,” *AIAA J.*, Vol. 51, No. 7, 2013, pp. 1695–1702.
- [19] Okamoto, M., Yasuda, K., and Azuma, A., “Aerodynamic characteristics of the wings and body of a dragonfly,” *J. Exp. Biol.*, Vol. 199, 1996, pp. 281–294.
- [20] Kunz, P. J., *Aerodynamics and design for ultra-low Reynolds number flight*, Ph.D. thesis, Stanford University, 2003.
- [21] Adams, N. A., “Direct numerical simulation of turbulent compression ramp flow,” *Theoret. Comput. Fluid Dyn.*, Vol. 12, 1998, pp. 109–129.
- [22] Ikeda, T., Sumi, T., and Kurotaki, T., “Interface conditions of finite difference compact schemes for computational aeroacoustics,” *AIAA J.*, Vol. 47, No. 11, 2009, pp. 2658–2665.
- [23] Itoh, N., Takagi, S., and Ikeda, T., “Instability and frequency selection of the wake behind a flat plate,” *Trans. Japan Soc. Aero. Space Sci.*, Vol. 55, No. 6, 2012, pp. 356–363.
- [24] Monkewitz, P. A., “The absolute and convective nature of instability in two-dimensional wakes at low Reynolds numbers,” *Phys. Fluids*, Vol. 31, 1988, pp. 999–1006.
- [25] McAlpine, A., Nash, E. C., and Lowson, M. V., “On the generation of discrete frequency tones by the flow around an aerofoil,” *J. Sound Vib.*, Vol. 222, No. 5, 1999, pp. 753–779.
- [26] Pier, B., Huerre, P., Chomaz, J.-M., and Couairon, A., “Steep nonlinear global modes in spatially developing media,” *Phys. Fluids*, Vol. 10, No. 10, 1998, pp. 2433–2435.
- [27] Pier, B. and Huerre, P., “Nonlinear self-sustained structures and fronts in spatially developing wake flows,” *J. Fluid Mech.*, Vol. 435, 2001, pp. 145–174.
- [28] Pier, B., “On the frequency selection of finite-amplitude vortex shedding in the cylinder wake,” *J. Fluid Mech.*, Vol. 458, 2002, pp. 407–417.
- [29] Chomaz, J.-M., “Global instabilities in spatially developing flows: non-normality and nonlinearity,” *Ann. Rev. Fluid Mech.*, Vol. 37, 2005, pp. 357–392.
- [30] Asai, M., Inasawa, A., Konishi, Y., Hoshino, S., and Takagi, S., “Experimental study on the instability of wake of axisymmetric streamlined body,” *J. Fluid Mech.*, Vol. 675, 2011, pp. 574–595.
- [31] Sunada, S., Yasuda, T., Yasuda, K., and Kawachi, K., “Comparison of wing characteristics at an ultralow Reynolds number,” *J. Aircraft*, Vol. 39, 2002, pp. 331–338.